Effect of the impurities O_2 or NO present in non-purified flue gas from oxy-fuel combustion processes for carbon capture and storage technology

Ana Pilar Melendo, Roberto Berbés, Sofía T. Blanco [*], Javier Fernández

Departamento de Química Física, Facultad de Ciencias, Universidad de Zaragoza, 50009 Zaragoza, Spain

ARTICLE INFO

ABSTRACT

CO_2/impurities cocapture in CCS technology allows reducing the purification costs and avoiding the emission of pollutants into the atmosphere. The viability of the transport by pipeline and the geological storage of the non-purified flue gas from oxy-fuel combustion of biomass and other processes, keeping the impurities O_2 or NO in the stream along with CO_2, is assessed considering thermodynamic and hydraulic aspects. For this, we experimentally determined, under CCS conditions, the density, vapor-liquid equilibrium, and speed of sound of three $CO_2 + O_2$ and $CO_2 + NO$ mixtures as binary models of the gas, and we calculated their Joule-Thomson coefficients from the experimental data. Additionally, we compared the values calculated for the determined properties using the equations of state EOS-CG, GERG-2008 and PC-SAFT to our results of $CO_2 + O_2$, validating all three equations for this system. For the $CO_2 + NO$ mixtures, only PC-SAFT could be applied, which was also validated using the parameters obtained in this work. Finally, we calculated several selected CCS parameters from our data and concluded that both O_2 and NO have negative effects on the transport and storage steps of this technology, which are negligible in the case of NO with the investigated concentrations.

1. Introduction

According to the International Panel of Climate Change, Global CCS Institute, and others (Friedmann et al., 2020; Global CCS Institute, 2021; IPCC, 2018), projections indicate that CO_2 net global emissions to the atmosphere (approximately 40 Gt in 2020) must be totally avoided by 2050 in order to achieve a 1.5 °C climate outcome.

The potential of CCS (carbon capture and storage) technology as a climate change mitigation tool has been recognized as a possible solution for many years, but its deployment has been slow. Nevertheless, given the reluctance of many countries to heavily reduce the consumption of fossil fuels in the short run and the tepid results of COP26 (COP26, 2021), CCS appears to be an essential technology (in conjunction with other mitigation options) to reach these targets. This method consists of the capture of anthropogenic CO_2 at emission facilities, its subsequent transport, typically by pipeline, and its underground storage into adequate reservoirs. Despite the COVID-19 crisis, many investments in this technology have been announced since the beginning of 2020, principally in Europe and the USA but also in Australia, New Zealand, China, Korea and the Middle East (IEA, 2020).

Unfortunately, Russia invaded Ukraine on 2022–02–24, strongly altering the geopolitical scenario and the global energy landscape. Given that the use of fossil fuels for energy production is the major source of greenhouse gas emissions, the future is very uncertain. Countries are returning to coal (Euronews, 2022-06–24), and the European Parliament modifies the green taxonomy to equate gas and nuclear with renewables (European Parliament News, 2022-07–06). In addition, the US Supreme Court has hobbled the EPA's (Environmental Protection Agency) authority over climate emissions (Nature news, 2022-06–30). In this scenario, advances in climate change mitigation are unavoidable, and considering that CCS technology makes it possible to minimize the negative effects of fossil fuels use and to develop zero-emissions energy production processes, broadening the technical knowledge regarding CCS is indispensable.

One of the ways to transition from fossil fuels to clean energies is the use of biomass or blends of biomass with fossil fuels as combustible, combined with CCS technology (BECCS or Bio-CCS). This technology is considered to produce negative emissions, and it is envisaged to have an important role in decarbonization strategic maps (Bui et al., 2017).

This paper is a part of a wider project whose main global objective is to evaluate the oxy-fuel combustion of biomass, pure or blended with

Nomenclature

a_i	Coefficients of the polynomials used to correlate the speed of sound values.		speed of sound values.
		p_{bubble}	Bubble pressure.
c	Speed of sound.	p_{dew}	Dew pressure.
d	Distance advanced by the stream along a pipeline.	p_{sat}	Saturation pressure.
D	Inner diameter of a pipeline.	T	Temperature.
k_{ij}	Binary interaction parameter (PC-SAFT EoS).	T_c	Critical temperature.
m	Segment number (PC-SAFT EoS).	$u(X)$	Combined uncertainty of a property X.
M/M_0	Normalized storage capacity of a reservoir.	Δv_c	Volume translation parameter (PC-SAFT EoS).
$\dot{M}/\dot{M}_0$	Normalized permeation flux of a plume in a reservoir.	v/v_0	Normalized velocity of the rising plume in saline aquifers.
MRD_X	Mean relative deviation for a property X.	x	Mole fraction.
$\overline{MRD}_X$	Global average mean relative deviation for property X.	Z	Compressibility factor.
		ε	Segment energy (PC-SAFT EoS).
n	Mole number.	η	Viscosity.
p	Pressure.	μ_{JT}	Joule-Thomson coefficient.
$p^{\#}$	Reference pressure in the polynomials used to correlate the	ρ	Density.
		σ	Segment diameter (PC-SAFT EoS).

coal, under different $O_2/CO_2/H_2O$ atmospheres without NO_x mitigation measures followed by the capture of the flue gas without further purification (CO_2/impurities cocapture) for transport and storage. The global conclusions will show the most expedient conditions for its integration into power production. Although the purification of anthropogenic CO_2 is technically accessible, its high cost makes it economically unaffordable (Anheden et al., 2004; Olajire, 2010). This high cost barrier is why CO_2/impurities cocapture appears to be an interesting option if the properties of the raw stream are adequate.

In this work, we evaluate the characteristics of the CO_2/impurity cocapture for three CO_2-rich binary mixtures containing O_2 or NO as impurities under conditions of interest for CCS. The compositions of the mixtures were CO_2 + 3.01 mol% O_2, CO_2 + 0.3012 mol% NO and CO_2 + 0.1991 mol% NO. These mixtures are considered binary mixture models for the raw flue gas without further purification from the above-cited BECCS or Bio-CCS processes (Lupiáñez et al., 2013a, 2013b; Pipitone and Bolland, 2009; Williams et al., 2012). Additionally, NO at the studied concentrations appears to be an impurity in emissions from other processes, such as gas engine combustion (Crismaru and Dragomir-Stanciu, 2015; Owczuk et al., 2018). Thus, the studied NO-containing mixtures are also binary mixture models for the flue gas for these processes without further purification. Binary mixture models are the first step on the study of more complex mixtures containing a higher number of impurities that would model the real flue gas. The effects of O_2 and NO as noncondensable impurities are evaluated and compared with those of other impurities of this type, such as CO or CH_4, that were previously studied by the authors (Blanco et al., 2012, 2014; Rivas et al., 2013). The study was carried out from the thermodynamic and hydraulic points of view without considering the possible chemical effects of the impurities.

Thus, density, ρ, vapor liquid equilibrium (VLE) and speed of sound, c, were experimentally determined for the studied mixtures at nine temperatures from 263 to 373 K and between atmospheric pressure and 30 MPa for densities and VLE and up to 190 MPa for speeds of sound. The p and T ranges include the conditions of interest for the CCS steps of transport, injection and storage (Li et al., 2011). Given the acoustic opacity of the mixtures at the operating frequency of 5 MHz, speeds of sound were determined by doping the mixtures with small amounts of methanol, a method previously tested by the authors and reported in preceding publications (Gimeno et al., 2017, 2018, 2019, 2021; Rivas et al., 2016). Despite doping, acoustic signals were not obtained in the low-pressure area of interest for CCS. For this reason, this work experimental data were extrapolated to lower pressures, and the results were validated using the GERG-2008 and the PC-SAFT equations of state, EoS (see Section 3.2).

We found in the literature a few experimental data for the CO_2 + O_2 mixture under similar conditions (Al-Siyabi, 2013; Fredenslund and Sather, 1970; Lasala et al., 2016; Mantovani et al., 2012; Westman et al., 2016), which are compared with those obtained in this work. No comparable data were found for the CO_2 + NO mixtures under similar conditions to those of this work, then our results fill this important gap in the literature since NO is a pollutant from combustion processes always present in the atmosphere.

From our experimental data, we calculated the Joule-Thomson coefficients, μ_{JT}, which describe the thermal behavior of the fluid under depressurization, for the mixtures CO_2 + 3.01 mol% O_2 and CO_2 + 0.3012 mol% NO at the studied pressures and temperatures.

CCS processes involve a wide range of compositions, pressures and temperatures, thus the availability of a predictive tool, such an equation of state (EoS), will be extraordinarily useful for this technology. The experimental data were utilized to evaluate three EoSs: EOS-CG (Equation of State for Combustion Gases, from Gernet and Span, 2016), developed for application to CO_2-rich mixtures of interest for CCS, among others; GERG-2008 (Groupe Européen de Recherches Gazières model, Kunz and Wagner, 2012), on which the above is based; and PC-SAFT (Perturbed-Chain Statistical Associating Fluid Theory equation of state, Gross and Sadowski, 2001), extensively used in the field of engineering.

Finally, from the presented experimental data and others from the literature, we calculated several design and operation CCS parameters. They were the minimum operational pressure, the pressure and density drops along a pipeline and the pipeline internal diameter, related to the transport; the permeation flux during injection; the storage capacity of the reservoir; and the velocity of the rising plume in saline aquifers. To assess the effect of the impurities on this technology, we compared the values of these parameters for the studied mixtures with those obtained for pure CO_2 and for the mixtures CO_2 + CO or + CH_4 with impurity concentrations similar to those used in this work. The storage parameters were also calculated for various real CCS saline aquifers (Table 1).

In the medium and long term, CCS can be vital in reducing CO_2 emissions where it is impossible to apply other measures, and from a circular economy perspective, to transform waste into a resource. This work focuses on the possibility of reduction of CO_2 emissions by means of the evaluation of the viability of transport and storage of CO_2-rich flue gases containing O_2 or NO as impurities, CO_2/O_2 or NO cotransport, coinjection and costorage, leading to a reduction in purification costs.

Table 1

Conditions of the saline aquifers studied in this work. ρ_{br} is the density of the brine.

Reservoir	Sleipner	Nagaoka	Frio	Nisku Fm. #1	Deadwood Fm. #2	Basal Cambrian Fm.	Snøhvit
p/MPa	10.3	11.9	15.2	17.4	23.6	27.0	29.0
T/K	317	319	329	329	338	348	373
Depth/m	1000	1100	1546	2050	2560	2734	2600
ρ_{br}/kg•m^{-3}	1017	999	1048	1076	1009	1137	1090
References.	[a], [b]	[a], [b]	[a], [b]	[b], [c]	[b], [d]	[b], [c]	[e], [f], [g]

[a]: Michael et al. (2010); [b]: Long and Chierici (1959); [c]: Bachu and Bennion (2008); [d]: Bachu (2013); [e]: IEAGHG (2015); [f]: Hansen et al. (2011); [g]: Grude et al. (2014).

2. Materials and methods

2.1. Materials

Table 2 collects the compositions of the mixtures object of this study, all of them supplied by Air Liquide.

The binary mixtures Mix 1 and Mix 2 were doped with methanol for speed of sound measuring purposes. CH$_3$OH (biotech grade, purity of 99.996% from gas chromatography) supplied by Sigma Aldrich was used immediately after being degassed.

2.2. Apparatus and methods

The hazards involved in the experimental part of this work are the high pressures reached inside the devices and those due to the reactivity and the toxicity of the studied impurities. O$_2$ is a strong oxidizing gas, and NO is a toxic gas that quickly reacts with air to produce NO$_2$, which is toxic as well. To avoid the risks consequence of these processes, a vacuum was created for at least two hours before putting the studied mixtures into the experimental installations, and leak detectors were used to find possible gas leaks after the investigated fluids entered into the apparatuses. In order to maintain safe the users from possible accidental throws, mobile polycarbonate transparent barriers were placed around the experimental facilities.

The guide suggested by NIST (JCGM 100:2008, 2008) was used to calculate the combined standard uncertainties of the experimental data obtained in this work.

mixtures, x_i, and the respective combined standard uncertainties, $u(x_i)$.

For the ternary mixture CO$_2$ + CH$_3$OH + O$_2$ (doped Mix 1), the mole fraction of methanol, x_{CH_3OH}, was determined by the relation

$$x_{CH_3OH} = \frac{n_{CH_3OH}}{n_{CH_3OH} + n_{Mix1}} \tag{1}$$

with

$$n_{CH_3OH} = \frac{(m_2 - m_1)}{M_{CH_3OH}} \tag{2}$$

$$n_{Mix1} = \frac{(m_3 - m_2)}{M_{Mix1}} \tag{3}$$

where m_1 is the empty cell mass, m_2 is the mass after methanol is added, and m_3 is the mass after Mix 1 is added into the variable-volume cell. M_{CH_3OH} is the molar mass of methanol, M_{Mix1} is calculated as $[M_{CO_2} \bullet (1 - x_{O_2,Mix1}) + M_{O_2} \bullet x_{O_2,Mix1}]$, M_{CO_2} and M_{O_2} are the molar masses of CO$_2$ and O$_2$, respectively, and $x_{O_2,Mix1}$ is taken from Table 2.

The mole fractions of CO$_2$ and O$_2$ in the CO$_2$ + CH$_3$OH + O$_2$ mixtures were determined by the following equations:

$$x_{CO_2} = \frac{n_{Mix1} \bullet (1 - x_{O_2,Mix1})}{n_{CH_3OH} + n_{Mix1}} \tag{4}$$

$$x_{O_2} = \frac{n_{Mix1} \bullet x_{O_2,Mix1}}{n_{CH_3OH} + n_{Mix1}} \tag{5}$$

$u(x_i)$, was estimated from (JCGM 100:2008, 2008):

$$u(x_i) = \sqrt{\left(\frac{\partial x_i}{\partial n_{CH_3OH}}\right)^2 u(n_{CH_3OH})^2 + \left(\frac{\partial x_i}{\partial n_{Mix1}}\right)^2 u(n_{Mix1})^2 + \left(\frac{\partial x_i}{\partial x_{O2,Mix1}}\right)^2 u(x_{O2,Mix1})^2} \tag{6}$$

The binary mixtures used for density and VLE measurements are detailed in Table 2. To measure the speeds of sound in Mix 1 and Mix 2 (Table 2), these mixtures were doped with $\approx$ 1 mol% of methanol given that the respective undoped mixtures were found opaque to the sound at the frequency of 5 MHz of our apparatus. The speed of sound of Mix 3 was not measured because the difference in impurity concentration between Mix 2 and Mix 3 is too low to be detected in our experimental device. A variable-volume cell with maximum volume of 0.51 L and maximum working pressure of 30 MPa was used to prepare the doped mixtures, introducing first the needed amount of methanol followed by Mix 1 or Mix 2. Methanol degassing was performed inside the variable-volume cell via intermittent vacuum with agitation. The mass of each introduced fluid was determined as the difference between the masses of the cell before and after its introduction. A Sartorius CCE 2004 mass comparator, which has a maximum weighing capacity of 2500 g and a repeatability better than 0.2 mg was used. When the doped mixtures were prepared, they were transferred to the experimental speed of sound installation. Detailed procedures can be found in previous publications (Gimeno et al., 2017). Table 3 shows the mole fractions of the doped

where $u(n_{CH_3OH})$ and $u(n_{Mix1})$ represent the standard uncertainties in the mole number of methanol and Mix 1, respectively, and $u(x_{O_2,Mix1})$ is the standard uncertainty of the O$_2$ mole fraction in Mix 1 given in Table 3. $u(n_{CH_3OH})$ was estimated as the square root of the sum of the square of the

Table 2

Compositions (mole fractions) of the studied binary mixtures and expanded uncertainties (coverage factor $k = 2$) in parentheses.

Components	Mix 1	Mix 2	Mix 3
CO$_2$	0.9699	0.996988	0.998009
O$_2$	0.0301 (0.00030)		
NO		0.003012 (0.000030)	0.001991 (0.000020)
Analysis Method	SM	SM	SM

SM: Supplier methods. The techniques reported were gas chromatography and electrolytic hygrometry.

Table 3

Mole fractions of the mixtures studied in the speed of sound installation, x_i, and their combined standard uncertainties, $u(x_i)$.

Component	Doped Mix 1		Doped Mix 2	
	x_i	$u(x_i)$	x_i	$u(x_i)$
CO_2	0.96000	0.00015	0.986893	0.000031
CH_3OH	0.010205	0.000011	0.0101257	0.0000099
O_2	0.02979	0.00015		
NO			0.002982	0.000030

standard deviation of the mole values calculated from the repetitive mass measurements after adding the methanol to the cell, plus the square of the estimated uncertainty due to the presence of impurities in that fluid. $u(n_{Mix1})$ was evaluated as the standard deviation of the mole values calculated from the repetitive mass measurements after adding Mix 1 to the cell. $u(x_{O_2,Mix1})$ was calculated as half of the standard expanded uncertainty (coverage factor $k = 2$) given for $x_{O_2,Mix1}$ in Table 2.

x_i and $u(x_i)$ for doped Mix 2 $CO_2 + CH_3OH + NO$ were obtained in the same way as those for doped Mix 1 and are given in Table 3.

The setup (provided by ARMINES) for the density and VLE measurements is designed for the accurate generation of $p - \rho - T$ data for fluids in the vapor and liquid phases and in the supercritical state. It is based on an Anton Paar DMA HPM vibrating-tube densimeter that is integrated in the installation (Fig. 1). The device works from 263 to 423 K of temperature, and the pressure reaches 70 MPa. Detailed explanations of the facility and procedures can be found in Blanco et al. (2014), Gimeno et al. (2017), and Velasco et al. (2011). After the acquisition of the installation, the fluid flow control was enhanced by the incorporation of electronically controlled electric motors to the valves that regulate the pressure variation during the measurements. The motors provided an optimization of the stability of the fluid flow, which was maintained below 0.005 MPa•s^{-1}, and ensured the thermodynamic quasi-equilibrium through quasi-static transformations (Bouchot and Richon, 1998).

The densimeter determines the vibration period, τ, with an

uncertainty of $u(\tau) = 2 \times 10^{-5}$ ms (provided by the manufacturer). The measuring temperature, i.e., the temperature of the fluid inside the vibrating tube, was measured by a 100 Ω platinum probe which was calibrated before this work by the Centro Español de Metrología (CEM, 2000). The estimated standard uncertainty in temperature was $u(T) = 0.006$ K and the variation of the temperature during the measurement of an $p - \rho - T$ isotherm was lower than ± 0.04 K. Two pressure transducers (GE Infrastructure model PTX 611), one of them for pressures below 6 MPa and the other from 6 to 70 MPa, were used to determine the pressure inside the densimeter. Both transducers were calibrated by the authors using a Wika CPH 6000 calibrator, and their accuracy was 0.025% over the entire scale. The combined standard uncertainty in pressure, $u(p)$, was 0.0020 MPa for $p < 6$ MPa and 0.024 MPa for 6 MPa $\leq p \leq 70$ MPa (Euramet, 2017). The vibrating tube was calibrated using the "forced path mechanical calibration" (FMPC) model, as the designers of the device recommend (Bouchot and Richon, 2001). The fluid used for calibration was pure CO_2, given that this compound is the principal component of the studied mixtures, and the calibration ranges covered from 263.15 to 373.15 K and up to 70 MPa (more details in the Supplementary material, p. S4).

The combined standard uncertainty in the density, $u(\rho)$, for each experimental $p - \rho - T$ point of the studied mixtures was calculated from the contributing uncertainties using the error propagation law (Gimeno et al., 2021; Supplementary material, p. S6). The uncertainty values accompany the experimental density data in the Supplementary material, Tables S1 and S2, and vary from 0.20 to 0.40 kg/m^3.

The $p - \rho - T$ data was analyzed by the tangents method as described in Gimeno et al., (2017, 2018), revealing the dew pressure and bubble pressure, p_{dew} and p_{bubble}, as well as the densities of the vapor, ρ_V, and liquid, ρ_L, phases in the VLE, and their respective combined standard uncertainties. The VLE data and their uncertainties are shown in Table S3.

$p - c - T$ isotherms were determined by means of a 5 MHz pulsed ultrasonic system (Fig. 2) (Rivas et al., 2016). The installation allows to work between 253 K and 473 K and from 0.1 MPa to 200 MPa, being $u(T) = 0.015$ K and $u(p) = 0.02$ MPa. CO_2 presents a high sound
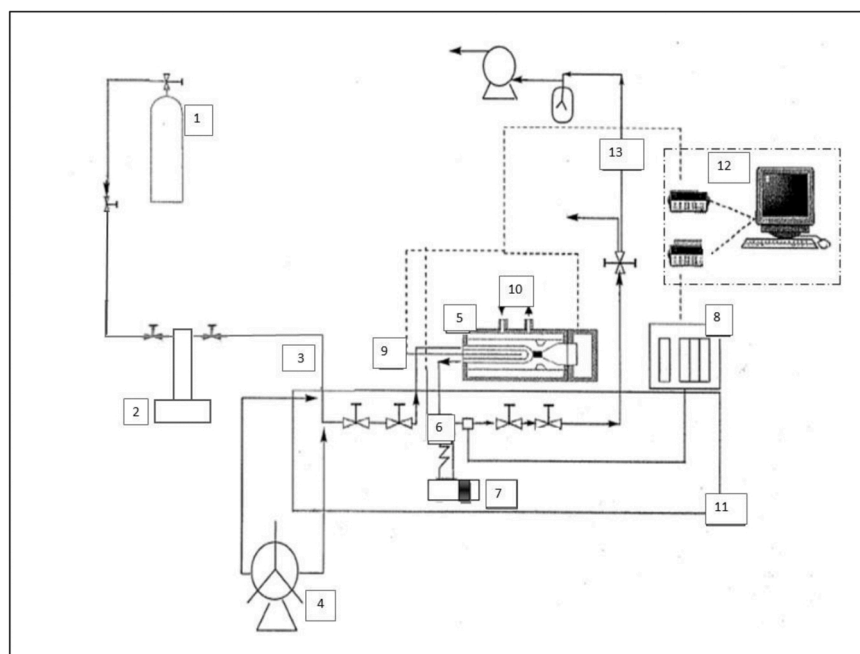

Fig. 1. Experimental facility for volumetric measurements: (1) feeding mixtures from Table 2; (2) syringe pump; (3) fluid entry; (4) screw pump; (5) vibrating tube densimeter; (6) densimeter way out; (7) safety disk; (8) pressure sensors; (9) temperature probe; (10) connected external liquid thermoregulated bath; (11) liquid thermoregulated bath; (12) evaluation unit and data acquisition; (13) evacuation and vacuum line.
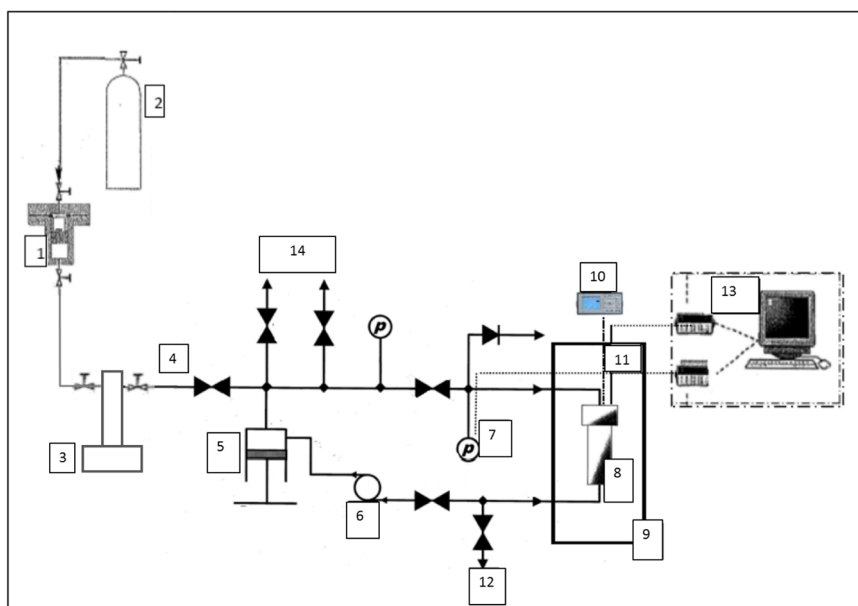Figure adapted from Bouchot and Richon (1998).

Fig. 2. Experimental facility for the measurement of the speed of sound: (1) variable-volume cell; (2) bottle of compressed nitrogen (used to push the piston of the variable-volume cell); (3) syringe pump; (4) fluid entry; (5) screw pump; (6) recirculation pump; (7) pressure sensor; (8) pressure vessel containing the ultrasonic cell; (9) thermostatic bath; (10) oscilloscope; (11) temperature probe; (12) drain line; (13) data acquisition unit; (14) evacuation line.

absorption at 5 MHz (Rivas et al., 2016), and as a consequence, pure CO_2 is opaque to the sound at this frequency, and the same occurs for the studied mixtures (Mix 1 and Mix 2) since O_2 and NO do not lower the sound absorption of the mixtures. The authors found in a previous work (Rivas et al., 2016) that the doping of CO_2 with approximately 1.0 mol% of CH_3OH allowed them to obtain proper signals along an adequate interval of pressures, with reproducible speed of sound values that showed mean deviations of 0.38% in regard to pure CO_2 (Span and Wagner, 1996). This value is smaller than the tolerance margin reported by the Span and Wagner EoS (reference EoS for this compound) under the studied conditions, which ranges between 0.5% and 2%. Based on these results, we measured the speed of sound of Mix 1 and Mix 2 doped with ≈ 1.0 mol% CH_3OH. This doping method was formerly applied by the authors in previous studies on CO_2-rich mixtures containing SO_2 (Gimeno et al., 2017, 2018, 2019, 2021; Rivas et al., 2016). In these systems, a lower concentration of methanol (≈ 0.8 mol%) was enough to achieve doping purposes, given that the presence of SO_2 in those mixtures lowered the sound absorption of CO_2 at 5 MHz and favored sound propagation through the fluid, which is not the case for O_2 and NO.

The combined standard uncertainty obtained for the experimental values of c, $u(c)$, was calculated using the following equation (Lin and Trusler, 2014):

$$(u(c))^2 = \left[(\partial c/\partial T)_{p,x} u_T\right]^2 + \left[(\partial c/\partial p)_{T,x} u_p\right]^2 + \left[(\partial c/\partial x)_{p,T} u_x\right]^2 + (u^*(c))^2$$

(7)

where $u^*(c)$ is the standard repeatability uncertainty.

To determine $u^*(c)$ for the $CO_2 + CH_3OH + O_2$ (doped Mix 1) and $CO_2 + CH_3OH + NO$ (doped Mix 2) systems, we prepared two mixtures with the same composition for each system, and we determined the $p - c - T$ isotherms for each mixture at 263, 293, and 313 K and pressures ranging from 10 to 197 MPa. Each isotherm was determined twice. The compositions of the mixtures and their uncertainties are shown in Table 3 and S4, and the measured c values are shown in Table S5. From these experiments, we obtained a $u^*(c) = 1.3 \times 10^{-3} \bullet c$ for $CO_2 + CH_3OH + O_2$, and the combined standard uncertainty of c was $u(c) = 1.3 \times 10^{-3} \bullet c$. For $CO_2 + CH_3OH + NO$, the results were $u^*(c) = 9.5 \times 10^{-4} \bullet c$, and $u(c) = 9.5 \times 10^{-4} \bullet c$. These values are comparable to those provided by the literature for mixtures (liquids or compressed

gases) using this type of apparatus (Ball and Trusler, 2001; Gimeno et al., 2017, 2018, 2019, 2021; Rivas et al., 2016).

3. Results and discussion

We present in the Section 3.1 the results obtained in this work, both experimental and calculated, and the discussion regarding the influence of each impurity on them. Section 3.2 develops a discussion on the predictive capability of the three evaluated equations of state. Section 3.3 studies the influence of the impurities O_2 or NO on several parameters related to the design and operation of the stages of transport (3.3.1), injection and storage (3.3.2) of the CCS technology, including their effect in seven selected real saline aquifers (Table 1). Along these sections, the comparison with the influence of other noncondensable impurities such as CO and CH_4 (Blanco et al., 2012, 2014; Rivas et al., 2013) is also discussed. The effect of NO is only evaluated on the minimum operational pressure and the storage capacity because the remaining parameters require viscosity values, which are not available for the $CO_2 + NO$ system.

3.1. Results

We measured 9 $p - \rho - T$ isotherms per mixture for Mix 1 ($CO_2 + 3.01$ mol% O_2), Mix 2 ($CO_2 + 0.3012$ mol% NO) and Mix 3 ($CO_2 + 0.1991$ mol% NO) (Table 2) at nominal temperatures of $T = 263.15$, 273.15, 283.15, 293.15, 303.15 and 313.15 K and pressures up to 20 MPa and at nominal temperatures of $T = 333.15$, 353.15 and 373.15 K and pressures up to 30 MPa. The experimental results, consisting of approximately 31,500 points, each data accompanied by its respective combined standard uncertainty, are presented in Table S1 (Supplementary material), and are also displayed in Fig. 3a and S2. Sets containing a lower number of points (approximately 50 per isotherm) are collected in Table S2 to make easier their use, along with their corresponding compressibility factors, Z, and their respective combined standard uncertainties.

The density of each mixture increases when pressure increases and temperature decreases. The three studied mixtures are subcritical at 263.15 K $\leq T \leq$ 293.15 K and their VLE are presented in Table S3 and in Fig. 4 and S3. These tables and figures include the values corresponding
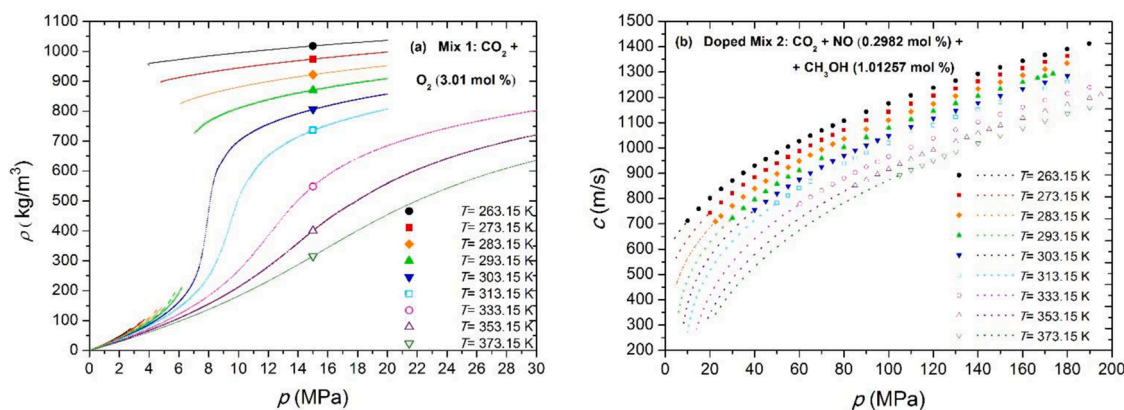
Fig. 3. (a) Experimental densities, ρ, for Mix 1. (b) Experimental (symbols) and extrapolated (dotted lines) speeds of sound, c, for doped Mix 2. Both versus pressure, p, and at the nominal temperatures T.
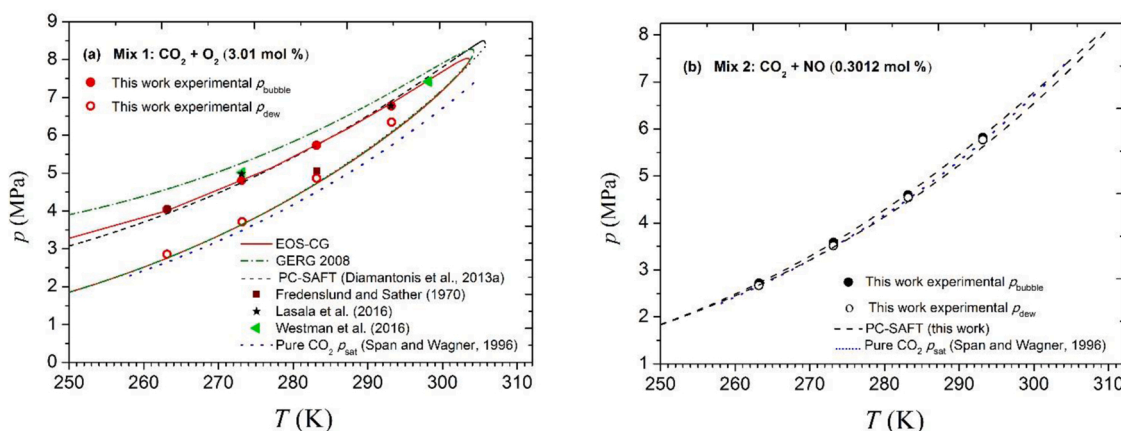

Fig. 4. Experimental and calculated VLE for the $CO_2 + O_2$ and $CO_2 + NO$ systems and for pure CO_2. Dew and bubble points for Mix 1 (a) and 2 (b).PC-SAFT parameters in (a) were taken from Diamantonis (2013a) and (b) uses parameters from this work (Table S10).

to pure CO_2 (Span and Wagner, 1996) for comparison. The rest of the studied temperatures were supercritical.

The $CO_2 + NO$ mixtures present continuity of the data at 303.15 K along the whole range of pressures studied (supercritical behavior), but we could not obtain reproducible results between approximately 5.8 and 7.3 MPa. For this reason, the densities in this interval of pressure are not reported for either mixture. It should be noted that 303.15 K is a supercritical temperature for the studied $CO_2 + O_2$ and $CO_2 + NO$ mixtures but is still subcritical for pure CO_2 (critical temperature $T_c = 304.21$ K, Gil et al., 2008).

Mix 1, which contains 3.01 mol% of a noncondensable impurity such as O_2, presents a density lower than that of CO_2 at all the studied conditions (Fig. S2). The mean relative deviation, MRD, between the densities of Mix 1 and those of pure CO_2 (Span and Wagner, 1996) at each temperature increases from 2.69% at 263 K to 7.46% at 303 K and then decreases as T increases, down to MRD = 4.01% at 373.15 K.

From the comparison of literature density data for $CO_2 + O_2$ (Al-Siyabi, 2013; Mantovani el al, 2012) with our results at equal temperature (283.15 and 293.15 K) or analogous (301.15 and 303.22 K vs. 303.15 K), we obtained that all of them are consistent (Fig. S4). They are not directly comparable given that the O_2 concentrations in the literature are ≈ 5 mol% (Al-Siyabi, 2013) and ≈ 6 mol% (Mantovani et al., 2012), but Mix 1 contains ≈ 3 mol%.

Fig. S5a shows the densities of Mix 1 ($CO_2 + 0.301$ mol% O_2) and of other CO_2–rich mixtures containing noncondensable impurities previously published by the authors (Blanco et al., 2012, 2014; Rivas et al., 2013), along with those of pure CO_2 (Span and Wagner, 1996), as a

function of the temperature and at selected pressures of transport and/or storage (8, 14, 20, and 30 MPa). The impurities were CO and CH_4 with concentrations similar to O_2 in Mix 1 ($CO_2 + 3.00$ mol% CO, and $CO_2 + 2.81$ mol% CH_4). All the studied impurities similarly reduce the density of the mixtures with respect to CO_2, except at 8 MPa from 303 to 313 K. Under these conditions, near the critical point of the mixtures, the impact of the three noncondensable impurities, in addition to being the highest, is clearly distinguishable, with CO showing the greatest density diminishing effect and O_2 showing the second greatest.

In the binary mixture $CO_2 + 0.3012$ mol% NO (Mix 2), the presence of NO reduces the density of the mixture, showing MRD values from 0.17% at 263 K to 0.60% at 333 K, without a clear trend of these values with T. The differences between the densities of Mix 2 and those of CO_2 are represented in Fig. S6a for each isotherm. The greatest deviations are observed at 303.15 K between 7 and 9 MPa, which are the studied conditions closest to the critical point of this mixture.

In relation to $CO_2 + 0.1991$ mol% NO (Mix 3), a decreasing effect of the density is observed with respect to CO_2 with MRD values, which does not show a clear trend with T and ranges from 0.16% at 333 K to 0.39% at 303 K. The greatest deviations ($\rho_{Mix3} - \rho_{CO_2}$) are obtained at 303.15 K from 7 to 9 MPa (Fig. S6b), similar to Mix 2, but with a lower value of the deviation at the minimum of the 303.15 K isotherm in Fig. S6. The values of the positive deviations in Fig. S6a and S6b are lower than or equal to the combined uncertainties estimated for the density of those points. In Fig. S5b, the densities of Mix 2 are compared with those of the previously studied mixtures $CO_2 + 0.40$ mol% CO and $CO_2 + 0.39$ mol % CH_4 (Blanco et al., 2012, 2014; Rivas et al., 2013) and with those of

pure CO_2 (Span and Wagner, 1996) at the studied temperatures and selected pressures (8, 14, 20, and 30 MPa). All of these densities are very close to each other at each temperature and pressure.

From the obtained $p-\rho-T$ experimental data, we determined the limits of the VLE, p_{dew} and p_{bubble}, and the densities of the phases at equilibrium, ρ_V (vapor) and ρ_L (liquid), along with their respective $u(p)$ and $u(\rho)$, for Mix 1, Mix 2 and Mix 3 (Table S3, Fig. 4 and S3). The tangents method was applied, as recommended by the authors of the experimental facility design and procedure (Bouchot and Richon, 1998) and as used in previous publications, where it is detailed (Gimeno et al., 2017, 2018, 2019, 2021). Fig. 4a presents our experimental p_{dew} and p_{bubble} values for Mix 1 along with data for $CO_2 + O_2$ mixtures with similar compositions from the literature (Fredenslund and Sather, 1970; Lasala et al., 2016; Westman et al., 2016) and p_{sat} for CO_2 (Span and Wagner, 1996). Given that the compositions are not exactly the same, good agreement is observed between our data and those from the literature at 263, 273 and 293 K, while the differences are higher at 283 K. No VLE literature data were found on $CO_2 + NO$ under similar pressure, temperature and composition conditions.

The presence of O_2 results in values for both the dew and bubble pressures of Mix 1 ($CO_2 + 0.301$ mol% O_2) that are higher than the saturation pressure of pure CO_2, p_{sat}, at each temperature (Table S3). The differences ($p_{bubble} - p_{sat}$) decreased with increasing temperature, with an average MRD value of 36%, while ($p_{dew} - p_{sat}$) increased with increasing temperature, and an average MRD value of 8% was obtained. Decreases from 2% to 8% are observed in ρ_L with respect to CO_2 and increases from 8% to 17% in ρ_V. For both densities, the differences compared to CO_2 increase as T increases. When comparing Mix 1 with the mixtures $CO_2 + 3.00$ mol% CO and $CO_2 + 2.81$ mol% CH_4 (Blanco et al., 2012, 2014) (Fig. S7a), we find that Mix 1 p_{dew} are somewhat higher than those of the other two mixtures at each temperature, with differences that increase with increasing temperature. Mix 1 p_{bubble}, instead, presents an intermediate value between those of the other two mixtures, and the difference decreases with increasing temperature.

The effect of NO in Mix 2 ($CO_2 + 0.3012$ mol% NO) and Mix 3 ($CO_2 + 0.1991$ mol% NO) is the increase in the bubble and dew pressures of the mixture with respect to CO_2 p_{sat} values, thus showing a noncondensable impurity behavior. The observed differences between the values for Mix 2 and those of CO_2 are 2.4% and 0.8% on average for p_{bubble} and p_{dew}, respectively; for Mix 3, the average differences are 1.6% and 0.7%, respectively. Regarding ρ_L, average decreases of 0.3% and 0.2% with respect to pure CO_2 are obtained for Mix 2 and Mix 3, respectively, and average increases of 1.4% and 1.5% in ρ_V. The effect of the presence of ≈ 0.2–0.4 mol% of each noncondensable impurity (NO, CO, CH_4) on the VLE of the binary mixtures represented in Fig. S7b is negligible with respect to CO_2 p_{sat}, except for $CO_2 + 0.40$ mol% CO p_{bubble}, which is clearly higher than CO_2 p_{sat} (Blanco et al., 2012, 2014).

In reference to the speed of sound measurements, we determined 9 $p-c-T-x$ isotherms per mixture for doped Mix 1 and doped Mix 2 (Table 3) at identical nominal temperatures to those used for the densities and up to 190 MPa. Mix 1 and Mix 2 were doped with ≈ 1.0 mol% of methanol to obtain acceptable sound signals in an adequate range of pressures. The results are presented in Table S6, Fig. 3b, and Fig. S8.

The variations of c in relation to p and T are similar to those shown by the density. The values of c in doped Mix 1 are lower than those found in pure CO_2, decreasing the differences as T increases; the MRD values per isotherm range from 2.35% to 1.24%. In the case of doped Mix 2, the c values are lower with respect to CO_2 at 353 and 373 K along the studied pressure range with MRD values of 0.18% and 0.15%, respectively. However, at the remaining isotherms, a reduction in the c values with respect to those of CO_2 is observed at pressures higher than ≈ 70–85 MPa, but an increase is obtained at lower pressures. In Fig. S9, the relative differences between the c values in the doped Mix 2 and in CO_2 are represented for each isotherm. The greatest variations are the reduction of c of 0.81% at 263 K and 190 MPa and the increase of 0.60% at 293 K and 30 MPa. There are published values for c on CO_2

+ 6.52 mol% O_2 (Al-Siyabi, 2013), which are not directly comparable with ours but are consistent. We did not find references in the literature about the speed of sound in the $CO_2 + NO$, $CO_2 + CH_3OH + O_2$ and $CO_2 + CH_3OH + NO$ systems.

To carry out the comparisons aimed at obtaining the uncertainties and to be able to obtain extrapolations to the low-pressure zone, we correlated the experimental c values of c at each temperature and composition as a function of pressure using the polynomial (Lin and Trusler, 2014):

$$(p - p^\#) = \sum_{i=1}^{3} a_i (c - c^\#)^i \tag{8}$$

being $p^\#$ an adequate reference pressure for each isotherm and $c^\#$ the corresponding speed of sound at $p = p^\#$. The values of $p^\#$ and the coefficients a_i in Eq. (8), as well as the MRD_c(%) for the experimental and fitted data, are shown in Table S7. The overall MRD_c values were 0.004% for doped Mix 1% and 0.005% for doped Mix 2, which are lower than the respective uncertainties for the experimental data.

Despite doping, we could not find acceptable sound signals in the low-pressure range, which is of interest for CCS technology. Therefore, in order to obtain suitable data in this zone, we used the fitted polynomials (Eq. 8, Table S7) to extrapolate the c results at low pressure at each temperature and composition (Table S8). The extrapolated data on $CO_2 + O_2$ were validated by comparison with the GERG-2008 EoS (Kunz and Wagner, 2012), which is the equation that better reproduces the experimental data of c in this mixture among the EoSs evaluated in this work, and the extrapolated data on $CO_2 + NO$ were validated by comparison with PC-SAFT (Gross and Sadowski, 2001) (see next section).

From our experimental and extrapolated values, we calculated the Joule-Thomson coefficient, μ_{JT}, for Mix 1 at nominal temperatures of 263.15, 273.15, 283.15, 293.15, 303.15, 313.15, 333.15, and 353.15 K, and for Mix 2 at the same nominal temperatures plus nominal 373.15 K (Table S9). μ_{JT} establishes how the stream thermally behaves during pipeline depressurization or release (operational or accidental) and during transport and injection, given that its sign determines whether the fluid cools up (positive) or warms up (negative) upon pressure drop, and its absolute value determines the magnitude of the thermal effect. The calculations were made via the following equations:

$$\mu_{JT} = \left(\frac{\partial T}{\partial p}\right)_H = \frac{V}{C_p}(\alpha_p T - 1) \tag{9}$$

$$C_p = \frac{\alpha_p^2 T}{\rho(\kappa_T - \kappa_S)} \tag{10}$$

where V is the molar volume, C_p is the heat capacity at constant pressure, and $\alpha_p, \kappa_T,$ and κ_S are the isobaric thermal expansivity, the isothermal compressibility and the isentropic compressibility, respectively. α_p was calculated from our experimental density data (263–373 K); to improve the calculations at the temperatures of the endpoints of the interval, values calculated using the GERG-2008 EoS (Kunz and Wagner, 2012) at 253.15 K and 383.15 K were also used. κ_T was obtained from the experimental ρ values, and κ_S was determined from the experimental ρ data and experimental and extrapolated c data. The results can be found in Table S9 and Fig. 5, where the μ_{JT} values for the binary mixtures are represented along with those for pure CO_2 (Span and Wagner, 1996) for comparison. At all the studied temperatures and pressures, the presence of 3.01 mol% O_2 in Mix 1 increases the values of μ_{JT} with respect to those for CO_2. The average deviations per isotherm increase as T increases from 263.15 to 313.15 K (0.057–0.334 K·MPa^{-1}) and decrease at 333.15 and 353.15 K (0.177 and 0.108 K·MPa^{-1}, respectively).

In Mix 2, an increasing effect of the presence of NO is observed in most of the T and p conditions studied, although μ_{JT} for Mix 2 and CO_2
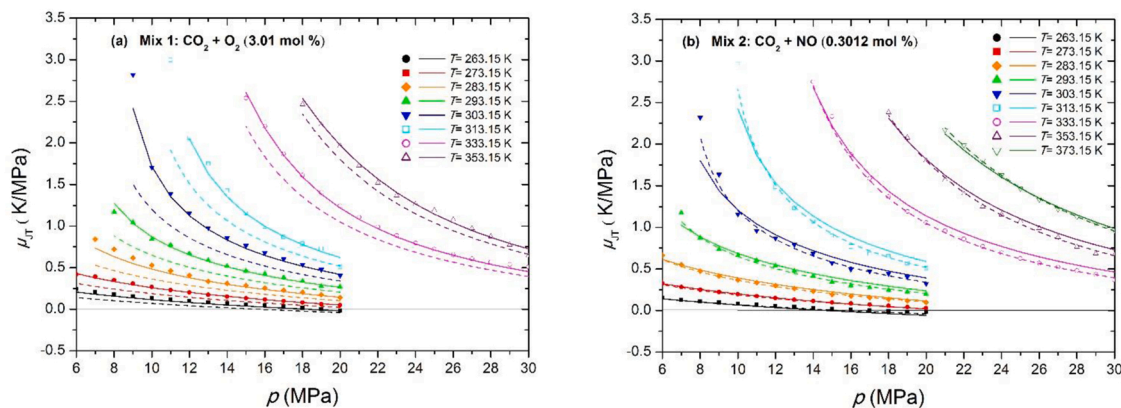
Fig. 5. Calculated Joule-Thomson coefficient, μ_{JT}, at several pressures, p, and temperatures, T, for Mix 1 (a) and 2 (b). Symbols, this work. Solid lines, GERG-2008 EoS (Kunz and Wagner, 2012) (a) or PC-SAFT EoS with coefficients from Table S10 (b). Dotted lines, pure CO_2 (Span and Wagner, 2016).

are very close.

μ_{JT} of Mix 1 and Mix 2 are positive at the studied T and p, with the exception of $T = 263.15$ K and $p \gtrsim 18.8$ MPa for Mix 1 and $T = 263.15$ K and $p \gtrsim 17.2$ MPa for Mix 2, where they change to negative values. These inversion pressures are higher than the inversion pressure of pure CO_2 at each temperature, 15.65 MPa (Span and Wagner, 1996). A positive μ_{JT} indicates that the fluid cools under depressurization, and a negative means that the fluid warms.

3.2. Comparison of the experimental data with those obtained from the EoS

The physical properties of anthropogenic CO_2 can significantly change due to the diverse compositions of the fluid and to the different values of T and p through the stages of CCS technology. Currently, there is no identified in the bibliography an optimal EoS to calculate the properties of the stream in the amplitude of conditions in which it can be found (Diamantonis et al., 2013b; Seevam et al., 2008; Wilhelmsen et al., 2012).

The EOS-CG mixture model (Gernert and Span, 2016) was developed to be applied to humid gases, gases from combustion processes and CO_2-rich mixtures of interest for CCS, and constitutes a positive breakthrough. This model, based on the GERG-2008 model (Kunz and Wagner, 2012), improves the prediction of phase boundaries of CO_2 mixtures along wide temperature and pressure ranges (Gernert and Span, 2016). EOS-CG and GERG-2008 were used to calculate the properties of Mix 1 as implemented in TREND 4.0 software (Span et al., 2019) and REFPROP 10 (Lemmon et al., 2018), respectively. Neither of the two equations have an available CO_2 + NO mixture model.

In addition, the PC-SAFT EoS (Gross and Sadowski, 2001), derived from statistical mechanics and widely used in the field of engineering and others, was also evaluated using VLXE software (Laursen, 2012). For the CO_2 + O_2 mixture, three different sets from the literature were used (Abolala et al., 2019, 2003) for the pure compound parameters, m (segment number), σ (segment diameter) and ε (segment energy), and for the binary interaction parameter, k_{ij}. Volume translation parameters, Δv_c, were not introduced since those authors did not use them.

We did not find in the literature PC-SAFT parameters for the CO_2 + NO binary mixture, either for pure NO. Consequently, we adjusted first the PC-SAFT parameters for NO, including Δv_c, from vapor pressure, saturated liquid density and heat capacity data of this compound taken from the Design Institute for Physical Properties (DIPPR) database available in VLXE software (Laursen, 2012). The overall MRD between the data from the literature and those calculated using the adjusted parameters were 2.15% for the vapor pressure, $8.76 \cdot 10^{-5}$% for the saturated liquid density and 0.97% for the heat capacity. The CO_2 pure compound parameters were sourced from Gross and Sadowski (2001).

The CO_2-NO binary interaction parameter was adjusted using our experimental results on p_{dew} and p_{bubble} for Mix 2 and Mix 3. The PC-SAFT parameters used in this work are collected in Table S10.

In the case of c measurements in doped Mix 1 and Mix 2, they were modeled while considering them as pseudobinary mixtures, i.e, the mole fractions of methanol were added to those of CO_2 (Gimeno et al., 2017, 2018, 2019, 2021).

The comparison of the predicted values to our experimental data allows us to evaluate the EoSs. The differences are given in terms of the MRD for each property X, MRD_X, and are presented in Tables S11 and S12 along with the global average values of the MRDs for each property X, $\overline{MRD_X}$. The relative deviations between the values calculated from the evaluated EoSs and the experimental properties obtained in this work are represented for each isotherm in Figs. S10 and S11.

The EOS-CG and GERG-2008 EoSs similarly reproduce the experimental values of the density of Mix 1 (CO_2 + 3.01 mol% O_2), with overall deviations of 0.80% and 0.79%, respectively. The maximum deviations for both EoSs are obtained at 303 K: 1.60% and 1.65%, respectively. PC-SAFT provides higher, but adequate, differences in the prediction of densities, with overall deviations of 1.64% (Set 1, Diamantonis et al., 2013a), 1.66% (Set 2, Abolala et al., 2019) and 1.46% (Set 3, Stoll et al., 2003). The EOS-CG is the equation that better reproduces the VLE data except for p_{dew}, which is slightly closer to the predictions of GERG-2008 and PC-SAFT with the parameters of Set 1. ρ_V is the VLE property whose predictions with all the evaluated EoS present higher deviations from the experimental data (from 5.44% to 10.31%), but the remainder of the experimental VLE properties are reproduced quite properly, with the exception of p_{bubble} by GERG-2008 EoS, which gives an average deviation of 8.68%.

The experimental speed of sound data for doped Mix 1 are slightly worse when reproduced by the EOS-CG (overall deviation of 0.82%) than densities, but the opposite is found for GERG-2008 with $\overline{MRD}_{c,exp} = 0.34$%. PC-SAFT with the parameters of Set 1 ($\overline{MRD}_{c,exp} = 2.63$%) and Set 3 ($\overline{MRD}_{c,exp} = 2.89$%) provides closer results to the experimental c data than those using the parameters of Set 2 ($\overline{MRD}_{c,exp} = 4.25$%), all of which are clearly worse than those obtained using the other EoSs. Given that GERG-2008 provided very good results for the speed of sound, we used this EoS to validate our extrapolations at low pressures. The deviations between the extrapolated values of speed of sound (Table S8) and those provided by the EoS are shown in Table S11, and their global average values ($\overline{MRD}_{c,ext}$) are 0.95% for EOS-CG, 0.67% for GERG 2008, and between 2.7% and 3.1% for PC-SAFT with the used sets of parameters.

PC-SAFT with the parameters of Table S10 (this work) predicts the

experimental densities of Mix 2 (CO_2 + 0.3012 mol% NO) and Mix 3 (CO_2 + 0.1991 mol% NO) with similar values of $MRD_{\rho,exp}$ per isotherm for both mixtures and reproduces the densities of the subcritical isotherms better than those at supercritical temperatures. The overall deviation is 1.08%. This equation properly reproduces the VLE data showing the highest deviations in the prediction of ρ_V, and no marked differences are obtained related to the composition of the mixtures. The experimental values of speed of sound in the doped mixtures are worse reproduced than the densities, $\overline{MRD_c}$ = 4.25% and $\overline{MRD_\rho}$ = 1.09% for Mix 2. The extrapolated values of the speed of sound in Mix 2 at low pressures (Table S8) were validated by means of this EoS. The deviations ($\overline{MRD_c}$ = 3.05%) were lower than those obtained for experimental c (Table S11).

We also assessed the capacity of the evaluated EoSs to reproduce μ_{JT} of Mix 1 and Mix 2 by comparing the values calculated using the EoSs to those obtained in this work. The differences, given as ADD, are presented in Table S13. EOS-CG and GERG-2008 EoS reproduce this property better than PC-SAFT, and in relation to PC-SAFT, parameters from Abolala et al. (2019) provide better results than the other two sets evaluated in this work.

The ADD values obtained in the predictions for Mix 2 using the PC-SAFT parameters adjusted in this work are similar to those obtained for Mix 1 with parameters from Abolala et al. (2019).

3.3. Influence of O_2 or NO on the transport, injection and storage stages of CCS technology

Anthropogenic CO_2 contains a variety of impurities, whose nature and concentrations determine the properties of the stream and, consequently, how the fluid behaves along the different operations of CCS technology.

In this section, we obtain several selected design and operation parameters related to the stages of transport, injection and storage of CCS technology, and we compare them with those obtained for CO_2 (Span and Wagner, 1996) to quantify and discuss the effect of the studied impurities, O_2 and NO. Additionally, the obtained CCS parameters are compared with those corresponding to CO_2-rich mixtures containing CO or CH_4 as noncondensable impurities at similar concentrations, as previously published (Blanco et al., 2012, 2014; Rivas et al., 2013).

The selected parameters for the transport step were the minimum operational pressure, p_{min}; the pressure and density drops along the pipeline, $p(d)$ and $\rho(d)$, respectively, being d the distance; and the inner diameter of the pipeline, D. The injection and storage parameters were calculated as normalized parameters, X/X_0, where X is the value for the mixture and X_0 is the value for pure CO_2. These parameters were the storage capacity of the reservoir, M; the velocity of the rising plume of the injected fluid inside deep saline aquifers, v; and the permeation flux, $\dot{M}$. The transport parameters were calculated at the temperatures of transport, ranging from 263 to 303 K, and pressures up to 20 MPa, while the injection and storage parameters were evaluated under storage conditions, i.e., nominal temperatures ranging from 303 to 373 K and pressures $p \geq 7$ MPa.

The equations used for calculating the related parameters are recommended by the literature (ElementEnergy, 2010; Vandeginste and Piessens, 2008; Wang et al., 2011) and are presented in Table S14. To apply these equations, we used the density data obtained in this work for the CO_2 + O_2 mixture and values from the literature for CO_2 + CO and CO_2 + CH_4 (Blanco et al., 2012, 2014; Rivas et al., 2013) and for CO_2 (Span and Wagner, 1996). The required viscosities were calculated for the CO_2 + O_2 mixture using an improved extended corresponding states method (Klein et al., 1997) implemented in the REFPROP 10.0 software (Lemmon et al., 2018), given that we did not find experimental data in the literature. For the CO_2 + NO mixture, neither experimental data nor adequate calculation methods were found, so only the minimum

operational pressure and the storage capacity, which do not require viscosity values, could be calculated.

The densities of the brines contained in the saline aquifers reported in Table 1, ρ_{br}, were estimated from the conditions of salinity, temperature and pressure in the respective reservoirs (Gimeno et al., 2017, 2019, 2021).

3.3.1. Influence of O_2 or NO on transport

Minimum operational pressure, p_{min}. To keep the fluid in a dense or supercritical phase is necessary to avoid biphasic flow and to optimize the transport capacity of the facilities. (Knoope et al., 2013; McCoy and Rubin, 2008). Therefore, transport and other operations must be carried out at pressures above the bubble pressure of the fluid at the working temperatures, with p_{bubble} plus an adequate safety margin stated as the minimum operational pressure. As demonstrated in previous publications (Blanco et al., 2012, 2014), the presence of noncondensable impurities, such as O_2, NO, CO or CH_4, increases the bubble pressure of the mixture at each given temperature with respect to CO_2 saturation pressure, p_{sat} (Span and Wagner, 1996), with differences that may be important depending on the nature and concentration of the impurities. Therefore, for the CO_2 + O_2 mixture with 3.01 mol% O_2, p_{bubble} increases by factors of 1.52, 1.38, 1.27, and 1.18 at nominal values of 263.15, 273.15, 283.15, and 293.15 K, respectively, with respect to p_{sat} of pure CO_2. This behavior is intermediate between those presented by the mixtures of CO_2 with CO or CH_4 with similar concentrations: factors 2.04, 1.72, 1.46, and 1.30 for CO_2 + CO (3.00 mol%) and factors 1.28, 1.21, 1.17, and 1.12 for CO_2 + CH_4 (2.81 mol%) at the same respective temperatures. Nevertheless, the presence of small concentrations of NO, such as 0.3012 or 0.1991 mol%, does not produce a significant increase in p_{bubble} with respect to pure CO_2 p_{sat}, presenting increment factors below 1.03 at both compositions and the studied temperatures. The p_{bubble} values of the CO_2 + NO mixtures are slightly lower than those corresponding to CO_2 + CH_4 (0.39 mol%), with differences lower than 1%, and lower than those for CO_2 + CO (0.40 mol%), with differences up to 13%. p_{bubble} for all the discussed mixtures are presented in Fig. S7 along with pure CO_2 p_{sat}.

The increase in p_{bubble} leads to an increase in the minimum operational pressure; hence, CO_2 + O_2 and CO_2 + NO mixtures are not favorable for this parameter with respect to the transport of pure CO_2 at all the studied transport temperatures.

Pressure and density drops along the pipeline, $p(d)$ and $\rho(d)$. For the pressure and density drop calculations, we considered a pipeline with an inner diameter of 20 in. (0.508 m) which transports a mass flow of 10 Mt/year (317.1 kg/s), whose roughness height is 0.00015 ft (4×10^{-5} m) and with an inlet pressure of 20.00 MPa. The pressure and density profiles along the pipeline for the mixture CO_2 + O_2 (3.01 mol%) and for pure CO_2 are represented in Fig. S12 at the studied transport temperatures. Fig. S13 shows the pressure and density at $d = 300$ km for CO_2 + O_2 (3.01 mol%), CO_2 + CO (3.00 mol%), CO_2 + CH_4 (2.81 mol%), and pure CO_2 as a function of the transport temperature. The presence of 3.01 mol% O_2 causes faster pressure and density drops along the pipeline than pure CO_2. At 300 km from the pipeline inlet, the pressure drops to 57.0%, 55.2%, 53.1%, 49.9% and 45.0% of the inlet pressure at 263, 273, 283, 293 and 303 K, respectively, and the density drops to 96.6%, 95.4%, 93.4%, 89.0% and 74.6% of the inlet density at the same respective temperatures (for pure CO_2, the pressure drops to 57.6%, 56.3%, 54.3%, 51.9%, and 48.4%, and the density drops to 97.0%, 96.2%, 94.6%, 91.9%, and 85.7%, respectively). This behavior is similar to those observed for the mixtures of CO_2 with CO or CH_4 with analogous concentrations, with similar drops of pressure and density except at the highest studied transport temperatures, 303 and 304 K, near the critical temperature of the mixtures, where the differences are higher.

Pipeline inner diameter, D. Fig. S14 presents the inner diameter of the pipeline, D, necessary to carry a mass flow of 10 Mt/year (317.1 kg/s) through a pipeline with a roughness height of 0.00015 ft for CO_2 + O_2 (3.01 mol%), CO_2 + CO (3.00 mol%), CO_2 + CH_4 (2.81 mol%) and pure

CO_2, as a function of the transport temperature, T, and at three selected pressures (8, 14 and 20 MPa). An average value of the pressure drop per meter of 31.8 Pa.m^{-1} was used. The presence of O_2, a noncondensable impurity, increases the diameter needed to transport a given flow, with differences that increase when temperature increases and pressure decreases. Thus, at the studied temperatures and 20 MPa, D is between 2 and 4 mm larger for $CO_2 + O_2$ (3.01 mol%) than for pure CO_2 and between 2 and 5 mm at 14 MPa. At 8 MPa, differences are also small at low temperatures but much more important at elevated temperatures, near the critical region of the mixture: 3 mm at 263 and 273 K, 4 mm at 283 K, 8 mm at 293 K and 43 mm at 303 K. For a pipeline of standard carbon steel, API 5 L X70, having an inner diameter of 508 mm (20 in.) and a wall thickness of 16 mm (McCoy and Rubin, 2008), an increase of 10 mm in the inner diameter while maintaining wall thickness, corresponds to an increase of approximately 3.9 tons of steel per km of pipeline (1.9%). An increase of 40 mm (inner diameter of 548 mm) requires a wall thickness of 17 mm (McCoy and Rubin, 2008) and entails an increase of approximately 30 tons of steel per km (15%). When comparing $CO_2 + O_2$ (3.01 mol%) with the mixtures $CO_2 + CO$ (3.00 mol%) and $CO_2 + CH_4$ (2.81 mol%), one can observe that the behaviors of the three mixtures with respect to D are very similar at all the studied temperatures and pressures (with a maximum difference of 1.2 mm) except at 303/304 K and 8 MPa, where the differences are much higher, and $CO_2 + O_2$ presents an intermediate behavior between the others. Thus, the $CO_2 + O_2$ mixture presents unfavorable characteristics with respect to pure CO_2 for this transport parameter, as well as the $CO_2 + CO$ and $CO_2 + CH_4$ mixtures do.

3.3.2. Influence of O_2 and NO on injection and storage

Normalized storage capacity, M/M_0. From the experimental density values of the binary $CO_2 + O_2$ and $CO_2 + NO$ mixtures, we obtained the influence of T, p and the composition of the anthropogenic CO_2 on the amount of the stored fluid in a specific reservoir. In Fig. S15a, the $M/M_0 - p$ isotherms for Mix 1 ($CO_2 + 3.01$ mol% O_2) show minimums, corresponding to a noncondensable impurity such as O_2. These minimums present increasing values and positions which shift to higher pressure when T increases. At pressures higher than ≈ 18 MPa, the influence of temperature and pressure on this parameter diminishes, and the highest storing efficiencies are reached for this mixture, with reductions of M of only ≈ 5–9% with respect to pure CO_2. Regarding NO, this impurity, with the studied concentrations, produces a small effect on M in most of the studied conditions. The reductions of M with respect to M_0 are lower than $\approx 0.5\%$ and $\approx 0.25\%$ for $CO_2 + 0.3012$ mol% NO (Fig. S15b) and $CO_2 + 0.1991$ mol% NO (Fig. S15c), respectively, at $T = 313.15$–373.15 K along the studied pressure range and at 303.15 K and pressures higher than 9 MPa. The higher reductions are found at 303.15 K and at pressures lower than 9 MPa, with maximum decreases

of $\approx 6.2\%$ and $\approx 4.8\%$ for Mix 2 and Mix 3, respectively.

The effects of the studied noncondensable impurities with concentrations lower than or equal to 0.4 mol% represented in Fig. 6a (NO, CO, CH_4) are similar to each other. They result in reductions of M that are less than $\approx 1.7\%$ with respect to pure CO_2 in the seven reservoirs of Table 1. The studied impurities with concentrations of 3 mol% (O_2, CO, CH_4) have unequal negative effects in the three shallower reservoirs, with O_2 leading to lower storage efficiencies in them. For the remaining reservoirs, the influence of the three impurities is similar and becomes less important, with reductions of M lower than 8% with respect to CO_2.

Normalized velocity of the rising plume in saline aquifers, v/v_0. Two different concentrations of the brine into the saline aquifer were considered: a concentrated brine with density $\rho_{br} = 1250$ kg/m^3 and a dilute brine with $\rho_{br} = 1025$ kg/m^3. The concentration of O_2 in Mix 1 (3.01 mol%) results in values of $v/v_0 > 1$ at all the considered T and p ranges (Fig. S16a and S16b), a characteristic effect of the presence of a noncondensable impurity in anthropogenic CO_2. This behavior weakens the safety of the reservoir because the retention of the fluid into the confinement diminishes as a consequence of the reduction of the stored fluid-brine contact. The unfavorable effect is less important in saline aquifers with concentrated brine (Fig. S16a) than with more diluted brine (Fig. S16b). In addition, the $v/v_0 - p$ isotherms exhibit values of v/v_0 close to unity at high temperatures and pressures, and deeper reservoirs are advisable confinements for this mixture.

In all the currently and recently operational aquifers considered (Fig. 6b), the addition to CO_2 of 0.4 mol% of the noncondensable impurities CO or CH_4 increases v with respect to CO_2 by as much as 5%. However, the addition of 3 mol% O_2, CO or CH_4 to CO_2 considerably increases v, giving values for this parameter, which diminishes as the depth of the reservoir increases. The mixtures with O_2 or CO or CH_4 exhibit similar values of v/v_0 except for Sleipner and Nagaoka. O_2 provides a value of v/v_0 markedly greater than that of CO in Sleipner and is similar to that in Nagaoka, while CH_4 with the same concentration, 3 mol%, is less unfavorable than O_2 and CO in all the studied aquifers.

Normalized permeation flux, $\dot{M}/\dot{M}_0$. This parameter allows us to evaluate the injectivity of the handled fluid and is calculated as the product of M/M_0 and the η_0/η relation (η_0 is the viscosity of pure CO_2). Most values of $\dot{M}/\dot{M}_0$ in Fig. S16c for $CO_2 + 3.01$ mol% O_2 are higher than the values of M/M_0 in Fig. S15a at the same p and T, which means that the viscosity of this mixture favors its injectivity under the studied conditions. Thus, the permeation flux of this mixture improves that of pure CO_2 at 303.15 K and $p \gtrsim 7.5$ MPa and 313.15 K and $p \gtrsim 9.5$ MPa.

The evaluated impurities give $\dot{M}/\dot{M}_0 \geq 1$ for the mixtures in the four shallower reservoirs studied (Fig. S17). In the Deadwood and Basal Cambrian reservoirs (deep aquifers), the $CO_2 + 3$ mol% CO mixture is the only one with $\dot{M}/\dot{M}_0 < 1$, and in Snøhvit, the deepest aquifer, none of the evaluated compositions improve the permeation flux of the
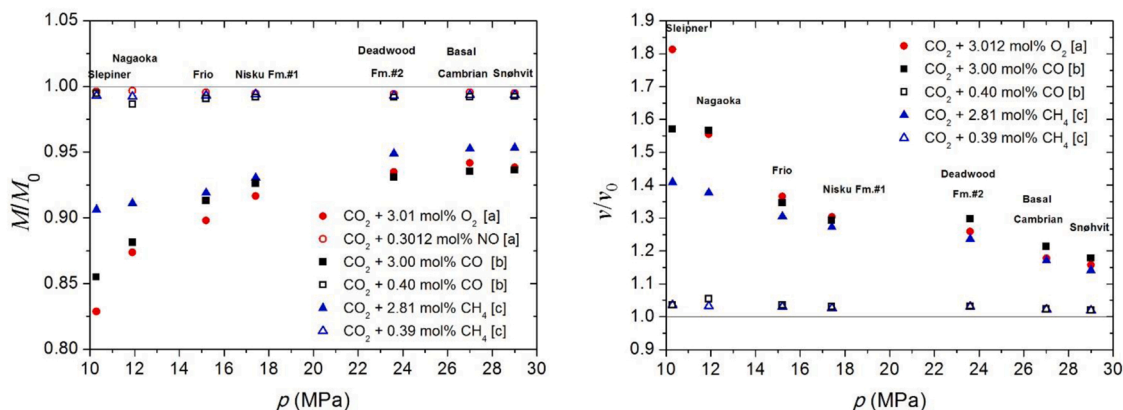

Fig. 6. (a) Normalized storage capacity, M/M_0, of the studied saline aquifers (Table 1). (b) Normalized rising velocity, v/v_0, in the same reservoirs. In both cases, different mixtures were considered. [a] This work; [b] Blanco et al. (2014); [c] Blanco et al. (2012).

mixtures with respect to CO_2.

4. Conclusions

We experimentally determined the density and VLE of the binary mixtures Mix 1 [CO_2 + 3.01 mol% O_2], Mix 2 [CO_2 + 0.3012 mol% NO] and Mix 3 [CO_2 + 0.1991 mol% NO] and the speed of sound of Mix 1 and Mix 2. The compositions of the mixtures correspond to binary models for the flue emissions from the oxy-fuel combustion of biomass (used alone or blended with coal) under different $O_2/CO_2/H_2O$ atmospheres without NO_x mitigation measures or further purification. In addition, CO_2 + NO binary mixtures could be considered model mixtures of gas engine combustion emissions. Temperatures and pressures ranged from 263 to 373 K and up to 30 MPa (densities) and up to 190 MPa (speeds of sound), which include the conditions of operation for the transport, injection and storage steps of the CCS technology.

Both impurities show noncondensable behavior. Their presence results in the decreasing of the density of the mixtures with respect to that of pure CO_2. Nominal 303.15 K, subcritical temperature for CO_2, is supercritical for the studied mixtures, and both the p_{dew} and p_{bubble} of the mixtures are higher than p_{sat} of pure CO_2 at the studied subcritical temperatures. The effects are clearly stronger in Mix 1, which contains 3 mol% of O_2, than in Mix 2 and Mix 3, with only 0.3 and 0.2 mol% of NO, respectively, in which are considered weak. The presence of O_2 decreases the speed of sound of Mix 1 with respect to pure CO_2 over the entire ranges of T and p, while NO diminishes the speed of sound of Mix 2 in the majority of the studied T and p but not in their entirety.

The calculated Joule-Thomson coefficients for Mix 1 and 2 are positive at the studied pressures and temperatures, except at 263.15 K and the highest of the studied pressures. They are clearly higher than those of pure et aCO_2 for Mix 1 and very close to them for Mix 2.

From our experimental data, we validated the EOS-CG, the GERG-2008 and the PC-SAFT EoSs for Mix 1. Globally, GERG-2008 better reproduces the density and speed of sound data than the others do, and EOS-CG is the best EoS to predict the VLE. For Mix 2 and Mix 3, we validated PC-SAFT using parameters adjusted in this work.

By using the experimental and calculated values obtained in this work, we evaluate the viability of the CO_2/O_2 or NO cotransport, costorage and coinjection, which would allow us to reduce the purification costs of the flue gas before transport. For that, we quantify the effect of the studied impurities in several transport, injection and storage technical parameters.

Thus, we found that the effect of O_2 is negative on all the studied transport parameters at all the studied temperatures and pressures: it increases the minimum operational pressure (p_{bubble}), the pressure and density drops along the pipeline, and the inner diameter necessary to transport a given mass flow. This behavior is similar to those of other noncondensable impurities, such as CO and CH_4, with similar concentrations, except near the critical region, where differences can be important.

CO_2/O_2 coinjection would be beneficial in the majority of current aquifers studied, and deep reservoirs are advisable for CO_2/O_2 costoring since the negative effects of this impurity in the storage capacity and the rising velocity of the plume are minimized in them. The effect of O_2, CO or CH_4 in the current aquifers of Table 1 is unequal for the high impurity concentrations (3 mol%) in the shallow reservoirs but similar for the rest of the studied conditions.

For Mix 2 and Mix 3, only the minimum operational pressure and the reservoir capacity could be calculated given the lack of viscosity data of the mixtures. Given the low concentrations, the effects of NO are so low that mixtures behave practically like pure CO_2.

We considered only thermodynamic and hydraulic aspects of the CO_2/impurity evaluated processes. Chemical effects due to the presence of impurities were not considered.

Declaration of Competing Interest

The authors declare that they have no known competing financial interests or personal relationships that could have appeared to influence the work reported in this paper.

Supplementary material

The Supplementary material contains tables and figures that present the experimental data, the results of the EoS modeling, and the results for the CCS calculated parameters, as well as detailed explanations about some procedures.

Appendix A. Supporting information

Supplementary data associated with this article can be found in the online version at doi:10.1016/j.psep.2023.02.086.

References

Abolala, M., Penyvandi, K., Varaminian, F., Hashemianzadeh, S.M., 2019. A comprehensive description of single-phase and VLE properties of cryogenic fluids using molecular-based equations of state. Fluid Phase Equilib. 494, 143–160. https://doi.org/10.1016/j.fluid.2019.04.038.

Al-Siyabi, I., 2013. Effect of impurities on CO_2 stream properties. Ph.D. Thesis. Heriot-Watt University.

Anheden, M., Andersson, A., Bernstone, C., Eriksson, S., Yan, J., Liljemark, S., Wall, C., 2004. Proceedings of the Seventh Greenhouse Gas Control Technologies Conference (GHGT-7), Vancouver, Canada, 2004.

Bachu, S., 2013. Drainage and imbibition CO_2/brine relative permeability curves at in situ conditions for sandstone formations in western Canada. Energy Procedia 37, 4428–4436. https://doi.org/10.1016/j.egypro.2013.07.001.

Bachu, S., Bennion, B., 2008. Effects of in-situ conditions on relative permeability characteristics of CO_2-brine systems. Environ. Geol. 54 (8), 1707–1722. https://doi.org/10.1007/s00254-007-0946-9.

Ball, S., Trusler, J., 2001. Speed of sound of n-hexane and n-hexadecane at temperatures between 298 and 373 K and pressures up to 100 MPa. Int. J. Thermophys. 22 (2), 427–443. https://doi.org/10.1023/A:1010770730612.

Blanco, S.T., Rivas, C., Bravo, R., Fernández, J., Artal, M., Velasco, I., 2014. Discussion of the influence of CO and CH4 in CO_2 transport, injection, and storage for CCS technology. Environ. Sci. Technol. 48 (18), 10984–10992. https://doi.org/10.1021/es502306k.

Blanco, S.T., Rivas, C., Fernández, J., Artal, M., Velasco, I., 2012. Influence of methane in CO_2 transport and storage for CCS technology. Environ. Sci. Technol. 46 (23), 13016–13023. https://doi.org/10.1021/es3037737.

Bouchot, C., Richon, D., 1998. Direct pressure− volume− temperature and vapor− liquid equilibrium measurements with a single equipment using a vibrating tube densimeter up to 393 K and 40 MPa: description of the original apparatus and new data. Ind. Eng. Chem. Res. 37 (8), 3295–3304. https://doi.org/10.1021/ie970804w.

Bouchot, C., Richon, D., 2001. An enhanced method to calibrate vibrating tube densimeters. Fluid Phase Equilib. 191 (1–2), 189–208. https://doi.org/10.1016/S0378-3812(01)00627-6.

Bui, M., Fajardy, M., Mac Dowell, N., 2017. Bio-Energy with CCS (BECCS) performance evaluation: efficiency enhancement and emissions reduction. Appl. Energy 195, 289–302. https://doi.org/10.1016/j.apenergy.2017.03.063.

CEM Centro Español de Metrología. Ministerio de Industria, T.y.C., 2000. Procedimiento TH-006 para la calibración de termómetros de resistencia de platino. Área de Temperatura.

COP26, 2021. UN climate change Conference. Glasgow 2021. https://www.un.org/en/climatechange/cop26. (Accessed 11 July 2022).

Crismaru, I.V., Dragomir-Stanciu, D., 2015. The influence of the flame stabilization air intake holes diameter on the no production in an industrial gas turbine. Procedia Technol. 19, 730–736. https://doi.org/10.1016/j.protcy.2015.02.103.

Diamantonis, N.I., Boulougouris, G.C., Mansoor, E., Tsangaris, D.M., Economou, I.G., 2013a. Evaluation of cubic, SAFT, and PC-SAFT equations of state for the vapor–liquid equilibrium modeling of CO_2 mixtures with other gases. Ind. Eng. Chem. Res. 52 (10), 3933–3942. https://doi.org/10.1021/ie303248q.

Diamantonis, N.I., Boulougouris, G.C., Tsangaris, D.M., El Kadi, M.J., Saadawi, H., Negahban, S., Economou, I.G., 2013b. Thermodynamic and transport property models for carbon capture and sequestration (CCS) processes with emphasis on CO2 transport. Chem. Eng. Res. Des. 91 (10), 1793–1806. https://doi.org/10.1016/j.cherd.2013.06.017.

ElementEnergy, 2010. pipeline infrastructure: an analysis of global challenges and opportunities. Final Rep. IEA Greenh. Gas. Program. CO2

Euramet, 2017. Guidelines on the Calibration of Electromechanical and Mechanical Manometers. Euramet Calibration Guide No.17. Version 3.0(04/2017).

Euronews, 2022-06–24. https://www.euronews.com/green/2022/06/24/all-the-european-countries-returning-to-dirty-coal-as-russia-threatens-to-turn-off-the-gas. (Accessed 07 July 2022).

European Parliament News, 06–07-2022. https://www.europarl.europa.eu/news/en/press-room/20220701IPR34365/taxonomy-meps-do-not-object-to-inclusion-of-gas-and-nuclear-activities. (Accessed 11 July 2022).

Fredenslund, A., Sather, G.A., 1970. Gas-liquid equilibrium of the oxygen-carbon dioxide system. J. Chem. Eng. Data 15 (1), 17–22. https://doi.org/10.1021/je60044a024.

Friedmann, J., Zapantis, A. Page, B., 2020. Net-Zero and Geospheric Return: Actions Today for 2030 and Beyond. Columbia University's Centre on Global Energy Policy and the Global CCS Institute. https://www.globalccsinstitute.com/resources/publications-reports-research/net-zero-and-geospheric-return-actions-today-for-2030-and-beyond/. (Accessed 11 July 2022).

Gernert, J., Span, R., 2016. EOS–CG: a Helmholtz energy mixture model for humid gases and CCS mixtures. J. Chem. Thermodyn. 93, 274–293. https://doi.org/10.1016/j.jct.2015.05.015.

Gil, L., Otin, S.F., Embid, J.M., Gallardo, M.A., Blanco, S., Artal, M., Velasco, I., 2008. Experimental setup to measure critical properties of pure and binary mixtures and their densities at different pressures and temperatures: determination of the precision and uncertainty in the results. J. Supercrit. Fluids 44 (2), 123–138. https://doi.org/10.1016/j.supflu.2007.11.003.

Gimeno, B., Artal, M., Velasco, I., Blanco, S.T., Fernández, J., 2017. Influence of SO2 on CO2 storage for CCS technology: evaluation of CO2/SO2 co-capture. Appl. Energy 206, 172–180. https://doi.org/10.1016/j.apenergy.2017.08.048.

Gimeno, B., Artal, M., Velasco, I., Fernández, J., Blanco, S.T., 2018. Influence of SO2 on CO2 transport by pipeline for carbon capture and storage technology: evaluation of CO2/SO2 cocapture. Energy Fuels 32 (8), 8641–8657. https://doi.org/10.1021/acs.energyfuels.8b01666.

Gimeno, B., Martínez-Casasnovas, S., Velasco, I., Blanco, S.T., Fernández, J., 2019. Thermodynamic properties of CO2+ SO2+ CH4 mixtures over wide ranges of temperature and pressure. Evaluation of CO2/SO2 co-capture in presence of CH4 for CCS. Fuel 255, 115800. https://doi.org/10.1016/j.fuel.2019.115800.

Gimeno, B., Velasco, I., Fernández, J., Blanco, S.T., 2021. Evaluation of the simultaneous presence of SO2 and CO as impurities in the carbon capture and storage technology. CO2/SO2/CO cocapture. Process Saf. Environ. Prot. 153, 452–463 ttps://doi.org/10.1016/j.psep.2021.07.041.

Global CCS Institute, 2021. Global Status of CCS Report 2021. https://www.globalccsinstitute.com/resources/global-status-report/. (Accessed 11 July 2022).

Gross, J., Sadowski, G., 2001. Perturbed-chain SAFT: an equation of state based on a perturbation theory for chain molecules. Ind. Eng. Chem. Res. 40 (4), 1244–1260. https://doi.org/10.1021/ie0003887.

Grude, S., Landrø, M., White, J., Torsæter, O., 2014. CO2 saturation and thickness predictions in the Tubåen Fm., Snøhvit field, from analytical solution and time-lapse seismic data. Int. J. Greenh. Gas. Control 29, 248–255. https://doi.org/10.1016/j.ijggc.2014.08.011.

Hansen, O., Eiken, O., Østmo, S., Johansen, R.I., Smith, A., 2011. Monitoring CO2 injection into a fluvial brine-filled sandstone formation at the Snøhvit field, Barents Sea, SEG Technical Program Expanded Abstracts 2011. Soc. Explor. Geophys. 4092–4096.

IEA, 2020. Energy Technology Perspectives 2020. Special Report on Carbon Capture Utilisation and Storage. https://www.iea.org/reports/ccus-in-clean-energy-transitions/a-new-era-for-ccus. (Accessed 11 July 2022).

IEAGHG, 2015. Review of offshore monitoring for CCS projects. IEAGHG Report 2015/2. https://ieaghg.org/docs/General_Docs/Reports/2015–02.pdf (Accessed 11 July 2022).

IPCC, 2018. The Intergovernmental Panel on Climate Change, Special Report on the Impact of Global Warming of 1.5°C. https://www.ipcc.ch/sr15/. (Accessed 11 July 2022).

JCGM 100:2008, 2008. GUM 1995 with minor corrections. Evaluation of measurement data —Guide to the expression of uncertainty in measurement. JCGM 2008. First edition 2008. Corrected version 2010.

Klein, S.A., McLinden, M.O., Laesecke, A., 1997. An improved extended corresponding states method for estimation of viscosity of pure refrigerants and mixtures. Int. J. Refrig. 20 (3), 208–217. https://doi.org/10.1016/S0140-7007(96)00073-4.

Knoope, M., Ramírez, A., Faaij, A., 2013. A state-of-the-art review of techno-economic models predicting the costs of CO2 pipeline transport. Int. J. Greenh. Gas. Control 16, 241–270. https://doi.org/10.1016/j.ijggc.2013.01.005.

Kunz, O., Wagner, W., 2012. The GERG-2008 wide-range equation of state for natural gases and other mixtures: an expansion of GERG-2004. J. Chem. Eng. Data 57 (11), 3032–3091. https://doi.org/10.1021/je300655b.

Lasala, S., Chiesa, P., Privat, R., Jaubert, J.-P., 2016. VLE properties of CO2 – based binary systems containing N2, O2 and Ar: experimental measurements and modelling results with advanced cubic equations of state. Fluid Phase Equilib. 428, 18–31. https://doi.org/10.1016/j.fluid.2016.05.015.

Laursen, T., 2012. VLXE ApS. Diplomvej. Scion-DTU, Denmark.

Lemmon, E.W., Bell, I.H., Huber, M.L., McLinden, M.O., 2018. Reference fluid thermodynamic and transport properties-REFPROP, NIST Standard Reference Database 23, 10.0 ed. U.S. Secretary of Commerce on behalf of the United States of America.

Li, H., Jakobsen, J.P., Wilhelmsen, Ø., Yan, J., 2011. PVTxy properties of CO2 mixtures relevant for CO2 capture, transport and storage: review of available experimental data and theoretical models. Appl. Energy 88 (11), 3567–3579. https://doi.org/10.1016/j.apenergy.2011.03.052.

Lin, C.-W., Trusler, J., 2014. Speed of sound in (carbon dioxide+ propane) and derived sound speed of pure carbon dioxide at temperatures between (248 and 373) k and at pressures up to 200 mpa. J. Chem. Eng. Data 59 (12), 4099–4109. https://doi.org/10.1021/je5007407.

Long, G., Chierici, G.L., 1959. Proceedings of the Fifth World Petroleum Congress, paper 16, Proceedings of the Fifth World Petroleum Congress. New York.

Lupiáñez, C., Díez, L.I., Romeo, L.M., 2013a. NO emissions from anthracite oxy-firing in a fluidized-bed combustor: effect of the temperature, limestone, and O2. Energy&Fuels 27, 7619–7627. https://doi.org/10.1021/ef4019228.

Lupiáñez, C., Guedea, I., Bolea, I., Díez, L.I., Romeo, L.M., 2013b. Experimental study of SO2 and NOx emissions in fluidized bed oxy-fuel combustion. Fuel Process. Technol. 106, 587–594. https://doi.org/10.1016/j.fuproc.2012.09.030.

Mantovani, M., Chiesa, P., Valenti, G., Gatti, M., Cpnsonni, S., 2012. Supercritical pressure-density-temperature measurements on CO2-N2, CO2-O2 and CO2-Ar binary mixtures. J. Supercrit. Fluids 61, 34–43. https://doi.org/10.1016/j.supflu.2011.09.001.

McCoy, S.T., Rubin, E.S., 2008. An engineering-economic model of pipeline transport of CO2 with application to carbon capture and storage. Int. J. Greenh. Gas Control 2 (2), 219–229. https://doi.org/10.1016/S1750-5836(07)00119-3.

Michael, K., Golab, A., Shulakova, V., Ennis-King, J., Allinson, G., Sharma, S., Aiken, T., 2010. Geological storage of CO2 in saline aquifers—a review of the experience from existing storage operations. Int. J. Greenh. Gas. Control 4 (4), 659–667. https://doi.org/10.1016/j.ijggc.2009.12.011.

Nature news, 2022-06–30. https://www.nature.com/articles/d41586–022-01796–8. (Accessed 11 July 2022).

Olajire, A.A., 2010. CO2 capture and separation technologies for end-of-pipe applications–a review. Energy 35 (6), 2610–2628. https://doi.org/10.1016/j.energy.2010.02.030.

Owczuk, M., Matuszewska, A., Wojs, M.K., Orliński, P., 2018. The effect of fuel type used in the spark-ignition engine on the chemical composition of exhaust gases. Przem. Chem. 97 (11), 1910–1915. https://doi.org/10.15199/62.2018.11.19.

Pipitone, G., Bolland, O., 2009. Power generation with CO2 capture: technology for CO2 purification. Int. J. Greenh. Gas. Control 3 (5), 528–534. https://doi.org/10.1016/j.ijggc.2009.03.001.

Rivas, C., Blanco, S.T., Fernández, J., Artal, M., Velasco, I., 2013. Influence of methane and carbon monoxide in the volumetric behaviour of the anthropogenic CO2: experimental data and modelling in the critical region. Int. J. Greenh. Gas. Control 18, 264–276. https://doi.org/10.1016/j.ijggc.2013.07.019.

Rivas, C., Gimeno, B., Artal, M., Blanco, S.T., Fernández, J., Velasco, I., 2016. High-pressure speed of sound in pure CO2 and in CO2 with SO2 as an impurity using methanol as a doping agent. Int. J. Greenh. Gas. Control 54, 737–751. https://doi.org/10.1016/j.ijggc.2016.09.014.

Seevam, P.N., Race, J.M., Downie, M.J., Hopkins, P., 2008. Transporting the Next Generation of CO2 for Carbon, Capture and Storage: The Impact of Impurities on Supercritical CO2 Pipelines, 2008 7th International Pipeline Conference. pp. 39–51.

Span, R., Beckmüller, R., Eckermann, T., Herrig, S., Hielscher, S., Jäger, A., Mickoleit, E., Neumann, T., Pohl, S.M., Semrau, B., Thol, M., 2019. TREND. Thermodynamic Reference and Engineering Data 4.0. Lehrstuhl für Thermodynamik, Ruhr-Universität Bochum.

Span, R., Wagner, W., 1996. A new equation of state for carbon dioxide covering the fluid region from the triple-point temperature to 1100 K at pressures up to 800 MPa. J. Phys. Chem. Ref. data 25 (6), 1509–1596. https://doi.org/10.1063/1.555991.

Stoll, J., Vrabec, J., Hasse, H., 2003. Vapor-liquid equilibria of mixtures containing nitrogen, oxygen, carbon dioxide, and ethane. AIChE J. 49 (8), 2187–2198. https://doi.org/10.1002/aic.690490826.

Vandeginste, V., Piessens, K., 2008. Pipeline design for a least-cost router application for CO2 transport in the CO2 sequestration cycle. Int. J. Greenh. Gas. Control 2 (4), 571–581. https://doi.org/10.1016/j.ijggc.2008.02.001.

Velasco, I., Rivas, C., Martinez-Lopez, J.F., Blanco, S.T., Otin, S., Artal, M., 2011. Accurate values of some thermodynamic properties for carbon dioxide, ethane, propane, and some binary mixtures. J. Phys. Chem. B 115 (25), 8216–8230. https://doi.org/10.1021/jp202317n.

Wang, J., Ryan, D., Anthony, E.J., Wildgust, N., Aiken, T., 2011. Effects of impurities on CO2 transport, injection and storage. Energy Procedia 4, 3071–3078. https://doi.org/10.1016/j.egypro.2011.02.219.

Westman, S.F., Stang, H.G.J., Løvseth, S.W., Austegard, A., Snustad, I., Ertesvåg, I.S., 2016. Vapor-liquid equilibrium data for the carbon dioxide and oxygen (CO2 + O2) system at the temperatures 218, 233, 253, 273, 288 and 298 K and pressures up to 14 MPa. Fluid Phase Equilib. 421, 67–87. https://doi.org/10.1016/j.fluid.2016.04.002.

Wilhelmsen, Ø., Skaugen, G., Jørstad, O., Li, H., 2012. Evaluation of SPUNG* and other equations of state for use in carbon capture and storage modelling. Energy Procedia 23, 236–245. https://doi.org/10.1016/j.egypro.2012.06.024.

Williams, A., Jones, J.M., Ma, L., Pourkashanian, M., 2012. Pollutants from the combustion of solid biomass fuels. Prog. Energy Combust. Sci. 38, 113–137. https://doi.org/10.1016/j.pecs.2011.10.001.